Calculated magneto-optical properties of pure and doped MnBi

1996 J. Phys.: Condens. Matter 8 8681

(http://iopscience.iop.org/0953-8984/8/44/017)

J. Phys.: Condens. Matter **8** (1996) 8681–8694. Printed in the UK

Calculated magneto-optical properties of pure and doped MnBi

J Köhler and J Kübler

Institut für Festkörperphysik, Technische Hochschule, D-64289 Darmstadt, Germany

Received 4 July 1996, in final form 2 September 1996

Abstract. The magneto-optical properties of MnBi show some striking features which we address here by calculating the Kerr spectra of pure MnBi, as well as of $MnBiX_{0.5}$ (X = Mn, Si, Al, O and Pt) and $MnBiX_{0.5}Y_{0.5}$ (X, Y) = (Al, Al) and (Al, O), (Pt, Pt). This system of compounds constitutes an example for which we demonstrate how much first-principles calculations can achieve and how our findings can be used to advance our knowledge of the origin of magneto-optical properties. Our calculations are based on the local density functional approximation (LDA) and the augmented spherical wave (ASW) band structure method including the scalar–relativistic and spin–orbit coupling terms to determine the effective one-electron energies and wavefunctions. From this we derive the inter-band and intra-band contributions to the optical conductivity tensor. Our results allow some statements concerning the connection of material properties with the magneto-optical properties. Thus, for instance, we are led to believe that oxygen plays an important role in explaining the experimental Kerr spectrum of pure MnBi. Furthermore, the measured enhancement of the Kerr angle in Al-alloyed MnBi is most probably not due to the occupation of interstitial sites by Al atoms. In contrast to this is Pt-alloyed MnBi, for which our calculations indicate that Pt partly occupies interstitial sites.

1. Introduction

Beginning with the work of Wang and Callaway [1] and through more recent developments by Ebert *et al* [2, 3], Uspenskii *et al* [4], Oppeneer *et al* [5, 6] and Halilov *et al* [7] it became clear that modern, self-consistent local-density-functional band-structure calculations can provide important insight into the magneto-optical properties of ferromagnetic metals and compounds. Thus, for instance in the case of FeCo films, calculations by Osterloh *et al* [8] together with experimental work by Weller *et al* [9] led to understanding of how the local atomic environment of the Fe and Co atoms influences the Kerr rotation spectrum. A further example is the case of $CoPt_3$ for which calculations of the polar Kerr rotation angle by Sticht *et al* showed two pronounced peaks at $E \approx 1.5$ eV and $E \approx 4.5$ eV in agreement with experimental data by Weller *et al* [10]. The emphasis of this work was to find out how the amplitude of the Kerr angle depends on the spin–orbit (SO) coupling. By manipulating the SO coupling constant these authors could establish that the UV peak originates from the SO coupling of the electrons that predominantly belong to the Pt atoms.

In this paper we turn to the ferromagnet MnBi which seems to be a promising candidate magneto-optical storage material because of its large Kerr rotation not only in the energy range of visible light but also in the UV region, its perpendicular magnetic anisotropy and its rectangular hysteresis loop [11]. Unfortunately, the MnBi grain size is large, leading to high medium noise. Moreover, the low-temperature phase (LTP) of MnBi at least partly

0953-8984/96/448681+14$19.50

undergoes a phase transition to the quenched high-temperature phase (QHTP) accompanied by liquid Bi phases, when the material is heated above the Curie temperature ($T_C \approx 630$ K) and cooled again during the writing process [12]. The QHTP of MnBi itself cannot be used as a storage material either, because it is thermally unstable. This means that it gradually changes back into the LTP by the reactions $Mn_{1.08}Bi \rightarrow MnBi + Mn$ and $Mn + Bi \rightarrow MnBi$ [12].

Attempts recently have been made to diminish the grain size and to mitigate the structural phase transition by suitable doping of MnBi [13–18]. The main features of the measured real Kerr rotation spectra that are of importance in this context are briefly summarized as follows.

Di *et al* [14] find for MnBi at room temperature in the real part of the Kerr angle two peaks at $E \approx 1.8$ eV and $E \approx 3.3$ eV with maximum values of $\Phi_K \approx -1.7^\circ$ and -1.4°, respectively. This was roughly confirmed by Huang *et al* [15]. Both groups coated the MnBi films with a SiO_2 layer before thermally annealing to protect the MnBi layer and to produce the desired orientation of the crystal.

In contrast to this is the experimental technique applied by Rüdiger *et al* [17], who obtained different Kerr rotation spectra by leaving out the SiO_2 layer [18, 19]. Because they measured their Kerr spectra from the substrate side, they had to compensate the enhancement of the Kerr rotation due to the quartz/MnBi interface by dividing the spectra by the index of refraction of the quartz substrate $n = 1.5$ [19]. They found two peaks at $E \approx 1.8$ eV and 3.5 eV in agreement with the foregoing authors but the maximum values are smaller: $\Phi_K \approx -0.7^\circ$ and -0.8°, respectively.

The experimental investigations of Al-alloyed MnBi by Rüdiger *et al* showed that it is possible to enhance the maximum values ($\Phi_K \approx -0.8^\circ$ and -0.9°) slightly compared to those of pure MnBi, whereas doping with Pt led to a distinct reduction [18]. In the case of Al-doped MnBi Huang found a maximum Kerr rotation angle of almost $\Phi_K \approx -2.0^\circ$ near $E \approx 2.0$ eV and $\Phi_K \approx -1.6^\circ$ at $E \approx 3.3$ eV [15]. This enhancement could not be reproduced by Sellmyer [16]. A theoretical investigation by Sabiryanov and Jaswal [20] indicated that Al-doping does not lead to larger Kerr rotation spectra. Another theoretical investigation recently appeared, by Oppeneer *et al* [21], which we will briefly discuss in section 3.

In an attempt to locate possible microscopic reasons for the occurrence of the UV peak as well as for the different experimental results we calculated the magneto–optical Kerr rotation spectra of pure MnBi and MnBi doped with Mn, Al, Si, O and Pt. In section 2 we summarize the calculational procedure and in section 3 the calculated Kerr rotation spectra are compared with experimental results. Section 4 contains a summary and our conclusions.

2. The calculational procedure

In this paper we consider the polar magneto-optical Kerr effect; that is, the direction of the macroscopic magnetization of the ferromagnetic material and the propagation direction of the linearly polarized incident light beam are perpendicular to the plane of the surface. Choosing the z axes normal to the surface and taking into account the symmetry of the compound we express the complex Kerr angle in terms of the xx and xy components of the optical conductivity tensor and obtain

$$\Theta_K := \phi_K + \mathrm{i}\,\varepsilon_K = \frac{-\sigma_{xy}}{\sigma_{xx}[1 + (4\pi\mathrm{i}/\omega)\sigma_{xx}]} \tag{1}$$

which follows from classical electrodynamics [4, 22–27]. Equation (1) can be used when the point group belonging to the crystal space group possesses at least one of the symmetry operations C_3, C_4, ... or S_3, S_4, ... [22] which is true for the NiAs structure as well as for those cases in which the interstitial sites are occupied. The components of the optical conductivity tensor are given by a sum of inter-band and intra-band contributions [28, 29]

$$\sigma_{\alpha,\beta}(\omega) = \sigma^{inter}_{\alpha,\beta}(\omega) + \sigma^{intra}_{\alpha,\beta}(\omega) \tag{2}$$

where the inter-band part contains direct one-electron transitions from occupied states $|\boldsymbol{k}, n\rangle$ to unoccupied states $|\boldsymbol{k}' = \boldsymbol{k},\ n' \neq n\rangle >$ and is given by

$$\sigma^{inter}_{\alpha,\beta}(\omega) = \frac{\mathrm{i}\, e^2}{m^2\, V} \sum_{\boldsymbol{k}\in BZ1.} \sum_{\substack{n,m \\ n\neq m}} \frac{f(E_{n,\boldsymbol{k}}) - f(E_{m,\boldsymbol{k}})}{E_{m,\boldsymbol{k}} - E_{n,\boldsymbol{k}}} \frac{\langle n, \boldsymbol{k}|p_\beta|m, \boldsymbol{k}\rangle\, \langle m, \boldsymbol{k}|p_\alpha|n, \boldsymbol{k}\rangle}{\omega - [(E_{m,\boldsymbol{k}} - E_{n,\boldsymbol{k}})/\hbar] + \mathrm{i}\delta}. \tag{3}$$

This expression is obtained by applying the Kubo formalism [30] to calculate the macroscopic electrical current induced by the electrical field of the light wave and by linearizing with respect to the electrical field strength [1]. (In other contexts these approximations are known as the RPA [31].)

The inter-band transitions are affected by scattering events which are phenomenologically described by using a finite life time; this is done by replacing the infinitesimal δ by a finite constant that is assumed to be independent of the detailed kind of inter-band excitation. In our calculations we use the value $\delta = 0.03$ Ryd ≈ 0.41 eV, which was in earlier investigations [5, 26] found to result in smooth curves without any loss of significant spectral features.

In practice we first calculate

$$A_{xx}(\omega) := \Re(\sigma^{inter}_{x,x}(\omega)) \qquad A_{xy}(\omega) := \Im(\sigma^{inter}_{x,y}(\omega)) \tag{4}$$

in the limit $\delta \to 0$. These expressions constitute the spectral functions of the retarded Green functions $\sigma^{inter,\,\delta}_{x,x}(\omega)$ and $\sigma^{inter,\,\delta}_{x,y}(\omega)$ corresponding to a finite relaxation time parameter $\delta > 0$. Therefore, the Green functions are given by a Kramers–Kronig transformation (generalized to finite values $\delta > 0$).

The numerical evaluation of the Brillouin-zone integration is performed by a linear (first-order) interpolation of the energy bands, a zeroth-order interpolation of the matrix elements and an analytical integration of the approximated integrand. The results obtained by this method agree with those obtained by an analytical tetrahedron method [5, 32], but the method used here is numerically more efficient. The calculation of the electron energy bands and corresponding wavefunctions is achieved by using the local density approximation (LDA) [33–35] and is numerically performed by the ASW method in the scalar–relativistic approximation [35, 36] including spin–orbit coupling in the variational procedure self-consistently. The intra-band contribution may be deduced either by transport theory [37] or by separating the contribution belonging to equal band indices $n = m$ from the result of the Kubo formalism and generalizing it to a finite lifetime parameter τ [28]. Both approximations lead to the Drude-like expression

$$\sigma^{intra}_{\alpha,\beta}(\omega) = \frac{\sigma^0_{\alpha,\beta}}{1 - i\,\omega\tau} \qquad \sigma^0_{\alpha,\beta} = \frac{\tilde{\omega}^2_{Pl,\,\alpha}\,\tau}{4\pi}\delta_{\alpha,\beta} \tag{5}$$

where the square of the plasma frequency is given by

$$\tilde{\omega}^2_{Pl,\,\alpha} = \frac{4\pi\, e^2}{V} \sum_n \sum_{\boldsymbol{k}\in BZ1.} \delta\big(E_{n,\boldsymbol{k}} - E_F\big)\big(v_\alpha(n, \boldsymbol{k})\big)^2 \qquad v_\alpha(n, \boldsymbol{k}) = \frac{1}{\hbar}\frac{\partial E_{n,\boldsymbol{k}}}{\partial k_\alpha}. \tag{6}$$

The lifetime parameter τ again describes scattering events and thermal properties of the crystal influencing the intra-band transitions. It is as before adjusted phenomenologically

and is chosen to be $\tau = 10^{-14}$ s corresponding to $\hbar/\tau = 0.0048$ Ryd $= 0.065$ eV, which is the correct order of magnitude for a large number of metals. Because the variation of this parameter within reasonable limits has very little effect on the optical conductivity for energies larger than 1 eV, the procedure just presented enables us to predict optical and magneto-optical properties of ferromagnetic compounds.

3. Results and discussion

The calculation of the band structure of pure MnBi in its low-temperature phase (LTP) proceeds from its hexagonal NiAs crystal structure shown in figure 1. As lattice constants the room temperature experimental values of $a = 4.290$ Å and $c = 6.126$ Å are used [38–40]. The values of the atomic sphere radii, employed in the ASW method, are given in table 1. They are chosen such that the atomic spheres are nearly neutral.

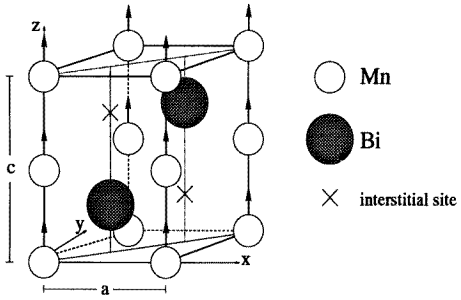

Figure 1. The unit cell of pure MnBi in its low-temperature phase (LTP) crystallizing in the NiAs structure. The interstitial sites (×) are (partly) occupied by additional atoms when simulating doped MnBi.

Table 1. Atomic sphere radii in ångström units used by the ASW band structure method to calculate the effective one-electron energies and eigenfunctions for pure and doped MnBi, respectively. The column labelled by 'empty' contains the radii of empty spheres located at unoccupied interstitial sites. The lattice parameters used are $a = 4.290$ Å and $c = 6.126$ Å (LTP) apart from for $MnBiMn_{0.5}$, for which $a = 4.390$ Å and $c = 6.000$ Å (QHTP) are employed.

	Atomic sphere radii Å						
Compound	Mn	Bi	Si	Al	O	Pt	Empty
MnBi	1.628	1.943					
$MnBiMn_{0.5}$	1.568	1.872					1.072
$MnBiSi_{0.5}$	1.638	1.830	1.269				1.072
$MnBiAl_{0.5}$	1.551	1.839		1.000			1.072
$MnBiO_{0.5}$	1.640	1.792			1.512		1.072
MnBiAl	1.606	1.871		0.988			
$MnBiAl_{0.5}O_{0.5}$	1.632	1.817		0.989	1.186		
$MnBiPt_{0.5}$	1.555	1.703				1.771	0.858
MnBiPt	1.510	1.572				1.629	

The band structure of MnBi (LTP) calculated for both spin directions separately using the scalar-relativistic ASW method is shown in figures 2 and 3. It agrees with the result of

de Groot *et al* [41]. Including the spin–orbit coupling term mixes the spin directions and leads to the complete band structure shown in figure 4.

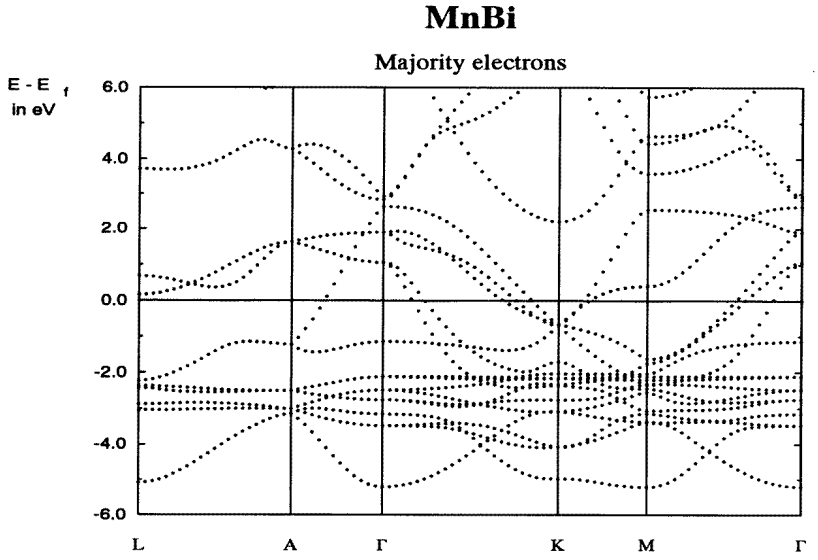

Figure 2. The electronic band structure of the majority electrons of MnBi along symmetry lines in the first Brillouin zone for the relevant energy range calculated by the scalar–relativistic ASW method. Labels used are according to Bradley and Cracknell [43].

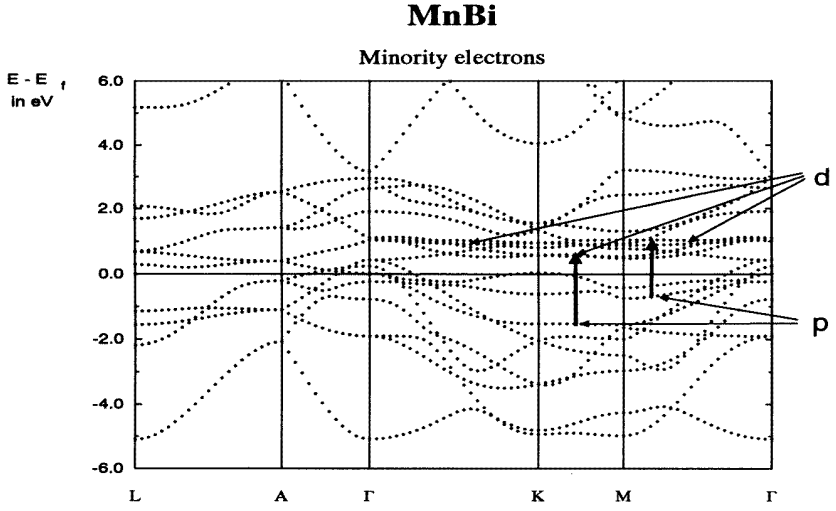

Figure 3. The electronic band structure of the minority electrons of MnBi along symmetry lines in the first Brillouin zone. The thin arrows indicate the Bi-p-↓ and Mn-d-↓ states; the thick vertical arrows symbolize possible direct inter-band transitions that are responsible for the large peak in the real Kerr rotation spectrum of pure MnBi at $E \approx 1.8$ eV.

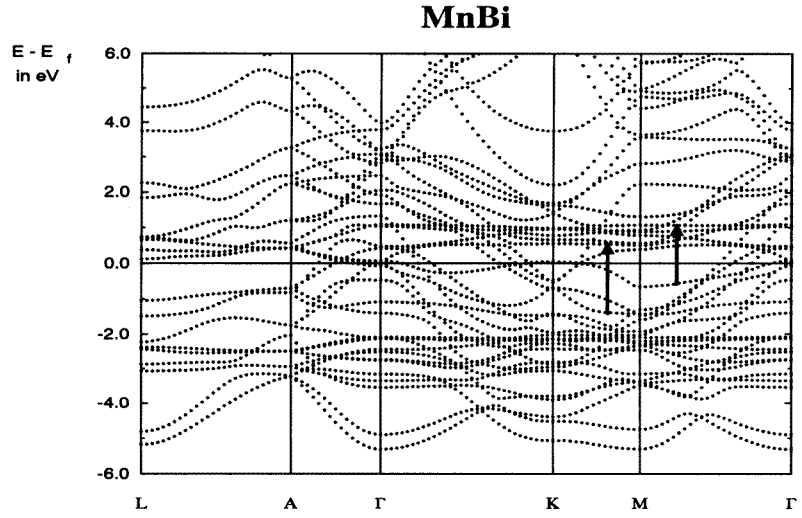

Figure 4. The electronic band structure of MnBi along symmetry lines in the first Brillouin zone for the relevant energy range calculated by the scalar–relativistic ASW method including the spin–orbit coupling term self-consistently. Labels used are according to Bradley and Cracknell [43].

The band structure indicates metallic behaviour and the magnetic moments are found to point along the c direction (which is the z direction), having the absolute values listed in table 2, in which also the orbital contributions to the magnetic moments are given. The total magnetic Mn moment brought out by our calculations, $m_{Mn} = 3.61\mu_B$, agrees with the result of de Groot *et al* [41] and is similar to the experimental value of $m_{Mn} = 3.84\mu_B$ published by Chen and Stutius [12]. Table 2: magnetic moments

To estimate the magneto-crystalline anisotropy of pure MnBi we calculated the total energy belonging to the configuration in which the magnetic moments are forced to point along the x axes perpendicular to the original direction. The difference between the total energies corresponding to the two configurations is $\Delta E = E_c - E_{\perp c} \approx -0.07$ mRyd per unit cell, which is of the correct sign. This result corresponds to a uni-axial anisotropy constant of $K_u \approx 1500$ kJ m^{-3}, that is close to the experimental results of $K_u = 1300$ kJ m^{-3} published by Chen and Stutius [12] and $K_u = 1160$ kJ m^{-3} measured by Guo *et al* [42], both belonging to LTP MnBi at $T = 300$ K.

Figure 5 shows the calculated real Kerr rotation spectrum of pure MnBi (full line) and experimental results of Di *et al* [14], Huang *et al* [15] and Fumagalli *et al* [19]. The experimental spectra feature two peaks corresponding to the energies $E \approx 1.8$–2.1 eV (first peak) and 3.3–3.5 eV (second peak), whereas the calculated spectrum consists of one maximum near $E = 1.7$ eV. The experimental results differ considerably in amplitude: Di and Huang found a Kerr rotation angle of $\Phi_K \approx -1.7^\circ$ (-1.5°) belonging to the first peak in agreement with the calculated value and $\Phi_K \approx -1.5^\circ$ (-1.3°) for the second peak. The maximum values measured by Fumagalli *et al* are smaller: $\Phi_K \approx -0.7^\circ$ for the first and $\Phi_K \approx -0.8^\circ$ for the second peak. In contrast to the first peak, the occurrence of a second peak in every measured spectrum is not brought out by our calculations for pure MnBi.

Oppeneer *et al* published two *ab initio* calculated Kerr spectra for the relaxation time parameter values $\delta = 0.04$ and $\delta = 0.02$ Ryd that show a pronounced peak at $E \approx 1.8$ eV

Table 2. Calculated absolute values of the total magnetic moments (μ_B/atom) for pure and doped MnBi, as well as their orbital and spin contributions. Because the Bi sites become inequivalent when occupying the interstitial sites, different magnetic moments result.

		Magnetic moments (μ_B/atom)		
Compound	Atom	m_S	m_L	m_{total}
MnBi	Mn	3.50	0.11	3.61
	Bi	−0.02	−0.03	−0.05
$MnBiMn_{0.5}$	Mn	4.24	−0.02	4.22
	Bi	−0.04/0.38	0.09/0.00	0.05/0.38
	Mn	4.48	−0.03	4.45
$MnBiSi_{0.5}$	Mn	3.15	0.09	3.26
	Bi	0.06/−0.01	0.00/0.00	0.06/−0.01
	Si	0.01	0.00	0.01
$MnBiAl_{0.5}$	Mn	2.99	0.01	3.00
	Bi	0.02/−0.23	−0.02/−0.02	0.00/−0.25
	Al	−0.02	0.00	−0.02
$MnBiO_{0.5}$	Mn	3.72	0.08	3.80
	Bi	0.05/−0.15	−0.01/0.00	0.04/−0.15
	O	0.07	0.00	0.07
MnBiAl	Mn	2.53	0.40	2.93
	Bi	0.16	−0.06	0.10
	Al	−0.009	−0.005	−0.014
$MnBiAl_{0.5}O_{0.5}$	Mn	2.83	0.06	2.89
	Bi	−0.05/−0.01	−0.01/0.00	−0.06/−0.01
	Al	−0.03	0.00	−0.03
	O	0.02	− 0.006	0.014
$MnBiPt_{0.5}$	Mn	4.02	0.1	4.12
	Bi	0.056/−0.161	0.004/0.001	0.06/−0.16
	Pt	0.30	−0.03	0.27
MnBiPt	Mn	3.49	0.025	3.52
	Bi	−0.19	0.022	−0.17
	Pt	−0.32	0.052	−0.28

with maximum values of $\Phi_K \approx -1.75^\circ$ and -2.22° respectively [21]. This agrees qualitatively with our spectrum, but the peak maximum values are larger than our result $\Phi_K \approx -1.5^\circ$. To explain the UV peak Oppeneer gave two arguments. On the one hand he observed a shoulder at the UV peak energy in the calculated MnBi spectrum, that is in our view not sufficient to explain the experimental data. On the other hand he constructed a hypothetical compound Mn_2Bi (Heusler C_1b crystal structure with a reasonably chosen lattice constant) having in mind that the samples had been prepared with excess Mn. The corresponding Kerr spectrum showed a peak at $E \approx 4.3$ eV which differed from the experimental peak energy by almost 1 eV.

At this time one might disregard the calculations as being of insufficient quality. Another possibility, however, is to accept the calculations as reflecting properties of idealized samples that only insufficiently mirror those of real samples. With this in mind we performed calculations to simulate MnBi doped with different substances that could possibly have been in contact with the MnBi layer during sample preparation. Such substances are Mn and Bi themselves, as well as Si and O in those cases in which a silicon-oxide layer was used. As futher doping substances we chose Al and Pt because recent experiments on Al-

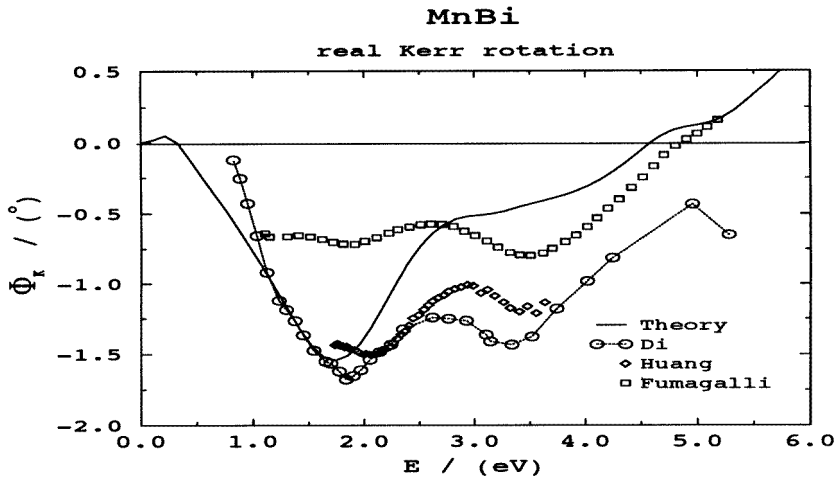

Figure 5. Kerr rotation spectra of pure MnBi in degrees: calculated (full line) and experimental results (symbols) by Di *et al* after [14] (○), by Huang *et al* [15] (◊), and by Fumagalli *et al* [19] (□). The calculated result consists of inter-band (relaxation-time parameter $\delta = 0.03$ Ryd) and intra-band contributions (the lifetime parameter $\tau = 10^{-14}$ s).

and Pt-alloyed MnBi have attracted considerable interest [13–18].

Because our calculational procedure requires periodic crystal lattices, we simulated doped MnBi crystals by occupying the interstitial sites of the NiAs structure (see figure 1). Furthermore, the lattice constants of the pure MnBi elementary cell were used, since measurements of the lattice parameters of pure and doped MnBi did not show any significant differences [13, 17, 44].

Because the quenched high temperature phase (QHTP) of MnBi consists of the MnBi crystal lattice (LTP) with interstitial sites partly filled by Mn atoms [41] and therefore corresponds to the $MnBiMn_{0.5}$ configuration, we chose for this case the lattice parameters of the QHTP, their being $a = 4.390$ Å and $c = 6.000$ Å [38–40].

The number of atoms actually built into the MnBi lattice is less than 10 at.%, although a larger amount of doping material is used during the sample preparation process [44]. This is considerably smaller than assumed in our calculations. Therefore our results exaggerate the influence of the doping substance and presumably also those features in the Kerr rotation spectrum that are brought about by the additional atoms of the doping material. This has to be kept in mind when comparing the calculated Kerr spectra with experimental data.

The radii of the atomic spheres are given in table 1. The results of these calculations are collected in table 3 in which we list the calculated plasma frequencies and in table 2 in which we list the spin and orbital contributions to the magnetic moments which we found to be ferromagnetically oriented along the c direction of the crystal. It is quite surprising that the calculated spin moments vary so much. The dominant reason for this (but not the only one) is the p–d hybridization that acts differently in the different cases. We discuss the example of $MnBiO_{0.5}$ later on.

Again, to estimate the magneto-crystalline anisotropy of $MnBiO_{0.5}$ as representative of the doped MnBi compounds, we also treated the configuration in which the magnetization direction points along the x axes. For the magneto-crystalline anisotropy energy we found $\Delta E = E_c - E_{\perp c} \approx -1.8$ mRyd per unit cell, which is substantially larger than the analogous

Table 3. Calculated plasma frequencies ($\hbar\omega_{Pl}$ for pure and doped MnBi.

Compound	$\hbar\omega_{Pl}$ (eV)
MnBi	3.4
$MnBiMn_{0.5}$	6.3
$MnBiSi_{0.5}$	2.3
$MnBiAl_{0.5}$	2.4
$MnBiO_{0.5}$	1.9
MnBiAl	2.4
$MnBiAl_{0.5}O_{0.5}$	2.6
$MnBiPt_{0.5}$	2.9
MnBiPt	2.7

result for pure MnBi.

In figure 6 we show the calculated Kerr angles for two simulations, one being for $MnBiMn_{0.5}$, the other one for $MnBiSi_{0.5}$. In the former case we found two peaks, one near 1.1 eV and the other near 3.7 eV. We note that, compared with the case of pure MnBi shown in figure 5, the peaks in figure 6 are considerably smaller. For $MnBiSi_{0.5}$ we found a single wide peak around $E = 1.5$ eV with a maximum value of $\Phi_K \approx -0.6^\circ$ smaller by 60% than that for pure MnBi.

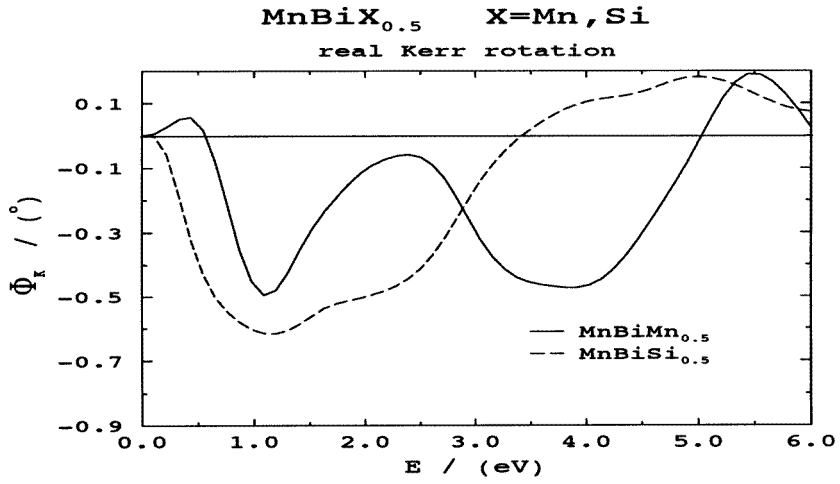

Figure 6. Calculated Kerr angles in degrees for $MnBiMn_{0.5}$ (full line) and $MnBiSi_{0.5}$ (broken line), using standard lifetime parameters for inter-band and intra-band contributions (see figure 5). In both cases the same single interstitial site of the MnBi elementary cell is occupied by a Mn and a Si atom. The lattice parameters of pure MnBi (LTP) are adopted for $MnBiSi_{0.5}$, whereas the lattice constants used for $MnBiMn_{0.5}$ are $a = 4.390$ Å and $c = 6.000$ Å, corresponding to the QHTP of MnBi after [38–40].

Figure 7 contains theoretical predictions of the Kerr rotation spectra when MnBi is doped with Al and O; these are in detail one interstitial site occupied by an Al atom ($MnBiAl_{0.5}$), by an O atom ($MnBiO_{0.5}$) and both interstitial sites occupied by two Al (MnBiAl) and one Al and one O atom, respectively ($MnBiAl_{0.5}O_{0.5}$). For comparison we also show experimental results corresponding to pure and Al-alloyed MnBi [18]. The simulation with one Al atom

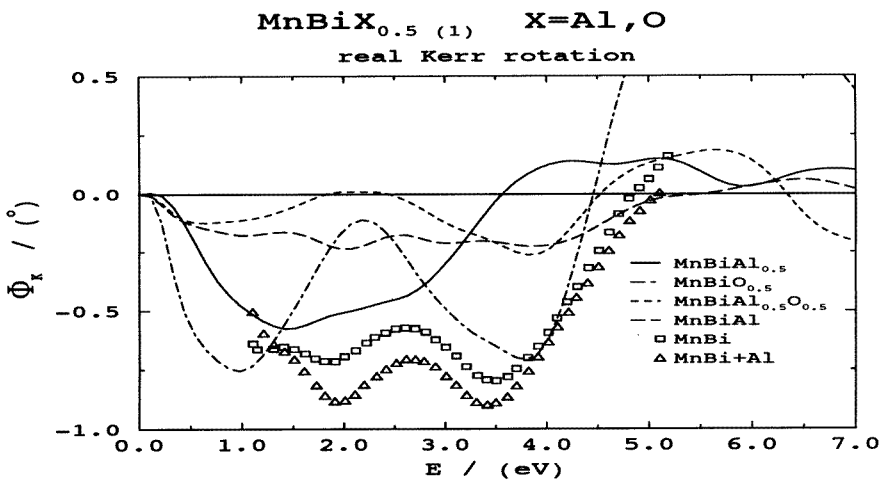

Figure 7. Energy-dependent Kerr rotation spectra for pure, Al-doped and O-doped MnBi. The lines correspond to calculated results for $MnBiAl_{0.5}$ (full), $MnBiO_{0.5}$ (chain), MnBiAl (long broken), and $MnBiAl_{0.5}O_{0.5}$ (broken). The symbols represent experimental results for pure MnBi by Fumagalli [19] (□) and for Al-alloyed MnBi by Rüdiger after [18] (△). The calculations are performed using the MnBi (LTP) lattice constants and standard lifetime parameters.

led to a broad maximum comparable to that calculated for the case of single-Si-doping. An additional Al atom reduces the amplitude of the Kerr rotation distinctly, so that these configurations cannot explain the measured spectrum of Al-alloyed MnBi.

In the case of occupation of a single interstitial site by an O atom, we obtained two peaks around $E = 1.0$ and $E = 3.7$ eV, having amplitudes of $\Phi_K \approx -0.75^\circ$. It is striking that this result is comparable to the experimental pure MnBi spectrum of Fumagalli *et al*: the calculated energy corresponding to the second peak differs from the measured one only by $\Delta E \approx 0.3$ eV and the amplitudes by about 7%. In the case of the first peak the latter are almost the same but the underlying energies differ by $\Delta E \approx 1$ eV. Very recent measurements by Rüdiger *et al* (1996, personal communication) could establish a third peak in the spectrum of pure MnBi at $E \approx 1.0$ eV, which possibly corresponds to the calculated $MnBiO_{0.5}$ peak at the same energy.

This result leads us to the conclusion that the sample not coated by an SiO_2 layer may contain a larger amount of oxygen than do SiO_2 coated samples. An explanation may be found in the preparation procedure; between the evaporation and thermal annealing process, occuring in different items of apparatus, the samples are in contact with air under normal conditions, whereby oxygen is possibly adsorbed which is distributed in the MnBi layer during the succeeding thermal annealing process [44]. Additional occupation of the remaining interstitial site by an Al atom reduces drastically the amplitude of the Kerr rotation spectrum, so that this configuration is probably not realized.

The calculated Kerr rotation spectra for one and both interstitial sites being occupied by Pt atoms are shown in figure 8. They are compared with measurements of Rüdiger *et al* performed for two different Pt concentrations [18]. The Kerr rotation spectrum belonging to the low-Pt-concentration case (the lc sample) may be understood by comparing it with the calculated $MnBiPt_{0.5}$ and $MnBiO_{0.5}$ spectra. These configurations seem to be realized in the lc sample.

The measured reduction in the amplitude of the Kerr rotation spectrum corresponding

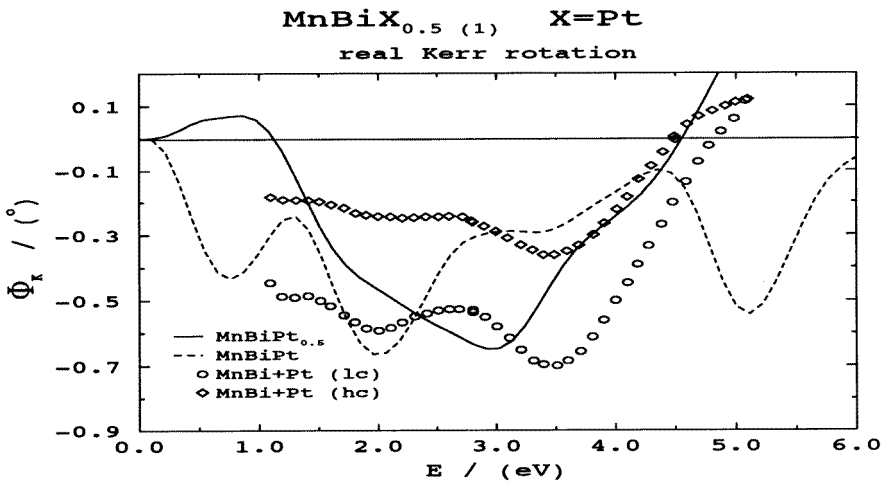

Figure 8. Kerr rotation spectra of Pt-alloyed MnBi in degrees. The lines represent the calculated results for $MnBiPt_{0.5}$ (full) and MnBiPt (broken), whereas the symbols represent measurements of Rüdiger *et al* for Pt-doped MnBi varying the Pt concentration: low (lc) (○), and high (hc) (◊) [18]. As before, the MnBi (LTP) lattice constants and the standard lifetime parameters were used to perform the calculations for one ($MnBiPt_{0.5}$) and both (MnBiPt) interstitial sites occupied by Pt atoms.

to a high Pt concentration (the hc sample) compared with that of the low-concentration case is not confirmed by the calculations. Because the shape of the calculated Kerr rotation spectrum of MnBiPt shows hardly any similarity with the measured spectra, the realization of this configuration seems to be most improbable. Thus, the measured reduction in the Kerr rotation angle for increasing Pt concentration cannot be explained by complete Pt occupation of the interstitial sites.

It is of importance to us to find the particular electron transitions responsible for the occurrence of the second peak in the real Kerr rotation spectrum; we, therefore, compared the partial density of states of the pure and O-doped MnBi plotted in the figures 9 and 10. The striking difference is the change in the density of the (Bi-p-↓) states. In pure MnBi the (Bi-p-↓) states form a maximum around $E - E_F = \Delta E = -1.6$ eV relative to the Fermi energy which is split into two less striking peaks with $\Delta E \approx -0.4$ and $\Delta E \approx -3$ eV in the case of $MnBiO_{0.5}$. Furthermore, the (O-p-↓) density of states has a wide maximum in the energy range $\Delta E \approx -3$ eV. The maximum density of (Bi-p-↓) states in $MnBiO_{0.5}$ is reduced compared to that belonging to the (Bi-p-↓) peak in MnBi.

The onset of (Mn-d-↓) states at $\Delta E \approx 0.3$ eV for pure MnBi and at $\Delta E \approx 0.6$ eV for $MnBiO_{0.5}$ then leads to a maximum number of (Bi(O)-p-↓) to (Mn-d-↓) transitions with transition energy of $E \approx 1.9$ eV (MnBi) and 1.0 and 3.6 eV ($MnBiO_{0.5}$), agreeing with the peak energies of the corresponding Kerr rotation spectra.

To identify the (Bi-p-↓) to (Mn-d-↓) transitions responsible for the peak in the real Kerr rotation spectrum of pure MnBi in the band structure plot, we have to separate the spin-↑ and spin-↓ states first. This may be done by switching off the spin–orbit coupling leading to the results shown in figures 2 and 3. The large (Mn-d-↓) final density of states corresponds to several flat bands above the Fermi energy that are indicated by the thin arrows in figure 3. The two peaks in the (Bi-p-↓) density of states, a smaller one at $E \approx -1.0$ eV and a

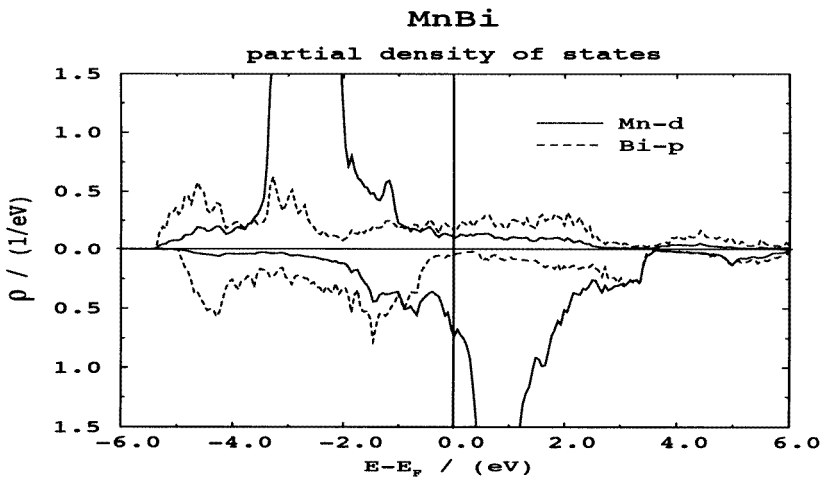

Figure 9. The calculated partial density of states of pure MnBi belonging to Mn-d (full lines) and Bi-p (broken lines), majority- and minority-spin states. The energy is scaled relative to the Fermi energy.

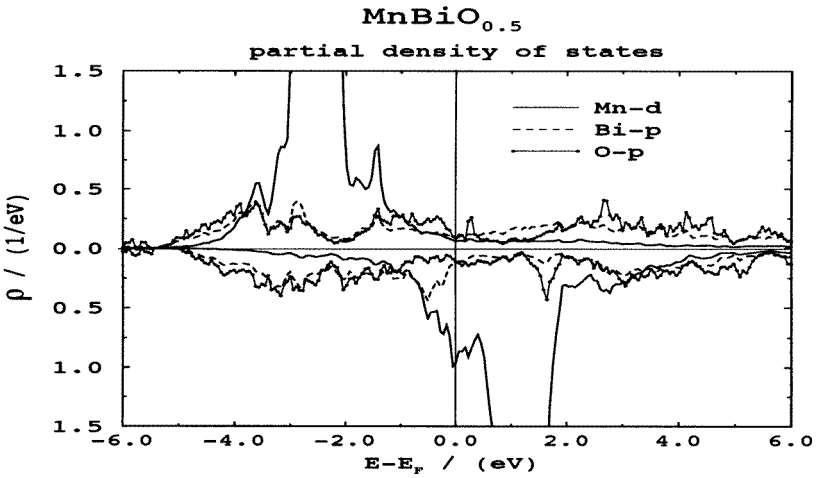

Figure 10. The calculated partial density of states of $MnBiO_{0.5}$ corresponding to the O-p, Bi-p and Mn-d majority- and minority-spin states.

more pronounced one near $E \approx -1.5$ eV, belong to the two rather flat bands below the Fermi energy, also marked in figure 3. Therefore the (Bi-p-↓) to (Mn-d-↓) direct inter-band transitions having a transition energy of about $\Delta E \approx 1.8$ eV, belonging to the large peak in the pure MnBi Kerr rotation spectrum, are probably those indicated by the thick vertical arrows in the spin-↓ and the combined band structure plot.

4. Summary and conclusions

Our results allow an interpretation of the main features of the Kerr rotation spectra of MnBi which may be summarized as follows. The first peak at $E \approx 1.8$ eV is due to states of the pure MnBi crystal and is mainly produced by (Bi-p-↓) to (Mn-d-↓) electron transitions. However, the observed second peak near $E \approx 3.5$ eV does, most probably, not originate from states of pure MnBi, but rather is probably due to O (Mn) doping. The electron transitions responsible for the occurrence of the second peak in $MnBiO_{0.5}$ are presumably the (Bi-p-↓) to (Mn-d-↓) transitions in combination with those starting from (O-p-↓) states.

The measured Pt-doped MnBi Kerr rotation spectrum for the low Pt concentration may be explained in terms of $MnBiPt_{0.5}$ and $MnBiO_{0.5}$ ($MnBiMn_{0.5}$). The Pt and O (Mn) atoms partly occupy the interstitial sites. In contrast, in the case of high a Pt concentration the measured Kerr spectrum cannot be explained by complete occupation of the interstitial sites by Pt atoms.

The measured increase in the Kerr rotation spectrum intensity for Al-alloyed MnBi is, most probably, not due to the occupation of the interstitial sites by Al atoms, because the calculation predicts drastically reduced amplitudes for this case. This is why we presume that the Al atoms basically do not penetrate the MnBi lattice, but probably constitute a separate layer.

Furthermore, the calculations show a reduction in the amplitudes of the real Kerr rotation spectra by about 50% (compared to MnBi) if one interstitial site is occupied by Mn, Si, Al, O and Pt and by about 80% in the cases that both interstitial sites are occupied by (Al,Al) or (Al,O). By generalizing these results we find the tendency that the more interstitial sites are occupied the smaller the amplitude of the corresponding Kerr rotation spectrum. The reason is the destruction of (Bi-p-↓) states by hybridization with the states of the additional atoms placed in the interstitial sites.

Acknowledgments

This work was supported by the German BMBF under grant TZ-PT-0223/94 13N6614 6. Helpful discussions with U Rüdiger are acknowledged.

References

[1] Wang C S and Callaway J 1974 *Phys. Rev.* B **9** 4897
[2] Ebert H *Physica* B 1989 **161** 175
[3] Ebert H and Akai H 1990 *J. Appl. Phys.* **67** 4798
[4] Halilov S V, and Uspenskii Y A 1990 *J. Phys.: Condens. Matter* **2** 6137
[5] Oppeneer P M, Maurer T, Sticht J and Kübler J 1992 *Phys. Rev.* B **45** 10 924
[6] Oppeneer P M, Sticht J, Maurer T and Kübler J 1992 *Z. Phys.* B **88** 309
[7] Halilov S V and Feder R 1993 *Int. J. Mod. Phys.* B **7** 683
[8] Osterloh I, Oppeneer P M, Sticht J and Kübler J 1994 *J. Phys.: Condens. Matter* **6** 285
[9] Weller D, Reim W, Ebert H, Johnson D D and Pinski F J 1988 *J. Physique Coll.* **49** C8 Suppl 12 41
[10] Weller D, Sticht J, Harp G R, Farrow R F C, Marks R F and Brändle H 1993 *Mater. Res. Soc. Sym. Proc.* **313** 501
[11] Chen D, Ready J F and Bernal E 1968 *J. Appl. Phys.* **39** 3916
[12] Chen T and Stutius W E 1974 *IEEE Trans. Magn.* **10** 581
[13] Wang Y J 1990 *J. Magn. Magn. Mater.* **84** 39
[14] Di G Q, Iwata S, Tsunashima S and Uchiyama S 1992 *IEEE Trans. Mang.* **7** (10) 792
[15] Huang D, Zhang X W, Luo C P, Yang H S and Wang Y J *J. Appl. Phys.* **75** 6351

[16] Sellmyer D J, Kirby R D, Chen J, Wierman K W, Chen J X, Liu Y, Robertson B W and Jaswal S S 1995 *J. Phys. Chem. Solids* **56** 1549
[17] Rüdiger U, Berndt H, Schirmeisen A, Fumagalli P and Güntherodt G 1995 *J. Appl. Phys.* **78** 5391
[18] Rüdiger U, Fumagalli P, Berndt H, Schirmeisen A and Güntherodt G 1996 *J. Appl. Phys.* **79** to be published
[19] Fumagalli P 1996 *Habilitationsschrift* Rheinisch Westfälische Universität Aachen
[20] Sabiryanov R F and Jaswal S S 1996 *Phys. Rev.* B **53** 313
[21] Oppeneer P M, Antonov V N, Kraft T, Eschrig H, Yaresko A N and Perlov A Y 1996 *J. Appl. Phys.* **80** to be published
[22] Wang X W 1993 *Dissertation* Iowa State University
[23] Bennett H S and Stern E A 1965 *Phys. Rev.* **137** 448
[24] Schönes J 1992 Magneto-optical properties of metals, alloys, and compounds *Mater. Sci. Technol.* vol 3A, ed K H J Buschow (New York: VCH) p 147
[25] Reim W and Schönes J 1990 *Ferromagnetic Materials* vol 5, ed E P Wohlfahrt and K H Buschow (Amsterdam: North-Holland) p 133
[26] Maurer T 1991 *Diplomarbeit* Technische Hochschule Darmstadt
[27] van Engen P G 1983 An experimental study of the magneto-optical properties of ferromagnetic alloys *Dissertation* Technische Universiteit Delft
[28] Mazin I I, Maksimov Ye G, Rashkeyev S N and Uspenskii Y A 1989 Microscopic calculation of the dielectric response function of metals *Metal Optics and Superconductivity* ed A I Golovashkin (New York: Nova)
[29] Uspenskii Y A and Khalilov S V 1989 *Sov. Phys.–JETP* **68** 588
[30] Kubo R 1957 *J. Phys. Soc. Japan.* **12** 570
[31] Rickayzen G 1980 *Green's Functions and Condensed Matter* (New York: Academic)
[32] Coleridge P T, Molenaar J and Lodder A 1982 *J. Phys. C: Solid State Phys.* **19** 6943
[33] Kohn W and Sham L 1965 *Phys. Rev.* A **140** 1133
[34] Barth U and Hedin L 1972 *J. Phys. C: Solid State Phys.* **5** 1629
[35] Kübler J and Eyert V 1992 Electronic structure calculations *Materials Science and Technology* vol 3A, ed K H J Buschow (New York: VCH) p 1
[36] Williams A R, Kübler J and Gelatt C D 1979 *Phys. Rev.* B **19** 6094
[37] Drude P 1892 *Ann. Phys. Chem., Lpz.* **46** 353
[38] Chen T 1974 *J. Appl. Phys.* **45** 2358
[39] Andresen A F, Hälg W, Fischer P and Stoll E 1967 *Acta Chem. Scand.* **21** 1543
[40] Villards P and Calvert L D 1985 *Pearson's Handbook of Crystallographic Data for Intermetallic Phases* vol 2 (Warrendale, PA: ASME) p 1468
[41] Coehoorn R and de Groot R A 1985 *J. Phys. F: Met. Phys.* **15** 2135
[42] Guo X, Chen X, Altounian Z and Stroem-Olsen J O 1993 *J. Appl. Phys.* **73** 6275
[43] Bradley C J and Cracknell A P 1972 *The Mathematical Theory of Symmetry in Solids* (Oxford: Clarendon) p 105